Meteorologische Zeitschrift, Vol. **20**, No. 4, 409-421 (August 2011)

Article

Analysis of a dryline-like feature in northern Germany detected by ground-based microwave profiling

DIETRICH SPÄNKUCH[1]*, JÜRGEN GÜLDNER[2], HANS STEINHAGEN and MICHAEL BENDER[3]

[1]Leibniz-Soziätet der Wissenschaften zu Berlin e.V., Germany
[2]Deutscher Wetterdienst, Meteorologisches Observatorium Lindenberg – Richard-Aßmann-Observatorium, Lindenberg, Germany
[3]Helmholtz-Zentrum Potsdam, Deutsches GeoForschungsZentrum GFZ, Germany

(Manuscript received July 22, 2010; in revised form April 18, 2011; accepted April 18, 2011)

Abstract

Two dryline-like humidity drops without considerable temperature change were detected by the ground-based microwave radiometer profiler (MWRP) at the Richard-Aßmann-Observatory Lindenberg (52.21°N, 14.12°E) on April 28, 2007. The detailed analysis of these two events includes cloud radar and radar wind profiler measurements at the site as well as data from the surface synoptic network and from integrated water vapour (IWV) maps derived from GPS. The first more pronounced humidity drop is part of a roughly 200 km long line that meets the criterion of a classical dryline or dewpoint front, namely of a moisture gradient larger 3.5 g m^{-3} per 100 km. This dewpoint front is ahead of an approaching cold front and is caused by strong downdraft induced by low tropospheric wind shear due to weakening of a midtropospheric high over Germany. It consisted in particular in two kernels of variable size depending on their stage. The fate of the kernels – migration, speed, unification and divorce – is described in detail. Their lifetime was a bit more than 9 hours. The second humidity drop at the site was observed after the passage of the cold front and was caused by dry advection behind the front. Both events are predicted by the numerical weather prediction model COSMO-EU of the German Weather Service to some extent.

Zusammenfassung

Am 28. April 2007 wurden mit dem Microwave Radiometer Profiler (MWRP) am Richard-Aßmann-Observatorium Lindenberg (52.21°N, 14.12°E) zwei ausgeprägte Feuchterückgänge in der Grenzschicht ohne nennenswerte Temperaturänderungen festgestellt. Solche Erscheinungen treten als Taupunktsfronten oder Drylines häufig im mittleren Westen der USA auf. Eine detaillierte Analyse der Feuchterückgänge wurde unter Nutzung von Wolkenradar- und Windprofilermessungen vor Ort sowie von Daten des synoptischen Beobachtungsmessnetzes und Karten der Verteilung des integralen Wasserdampfgehalts, abgeleitet aus GPS-Daten, vorgenommen. Der erste, intensivere Feuchterückgang gehört zu einer etwa 200 km langen Taupunktsfront, die sich vor einer heranrückenden Kaltfront im Ergebnis stark absinkender trockener Luft gebildet hat. Die Absinkbewegung wird verursacht durch niedertroposphärische Windscherung als Folge eines über Deutschland liegenden sich auflösenden Höhenhochs. Die präfrontale Dryline besteht im Wesentlichen aus zwei Kernen, deren Größe von deren Entwicklungsstand abhängt. Das Schicksal dieser Kerne – Wanderung, Wanderungsgeschwindigkeit, Vereinigung und Trennung – wird ausführlich dargestellt. Der präfrontale Charakter und die Stärke des Feuchtegradienten der Erscheinung entsprechen den Merkmalen einer Dryline. Der zweite Feuchterückgang wurde nach dem Durchgang der Kaltfront beobachtet und ist das Ergebnis von Advektion trockener Luft nach der Kaltfront. Beide Vorkommnisse wurden in gewissem Grad durch das numerische Vorhersagemodell COSMO-EU prognostiziert.

1 Introduction

The continuous monitoring of the atmospheric boundary layer (ABL) is vital for many meteorological applications. Microwave radiation emitted by the atmosphere contains information on temperature, water vapour, and liquid cloud water (WESTWATER et al., 2005). Ground-based microwave radiometer profiler (MWPR) provide vertical thermodynamic profiles up to 10 km in both clear and cloudy conditions with high temporal resolution and sufficient accuracy in the lower troposphere (GÜLDNER and SPÄNKUCH, 2001) and are therefore well suited for ABL monitoring (KNUPP et al., 2009; GÜLDNER et al., 2009). Combined with other remote sensing measurements, MWRP observations provide essential information for a multitude of applications (LÖHNERT et al., 2004; HEWISON, 2007; ILLINGWORTH et al., 2007; TURNER, 2007). Quasi continuous monitoring of the temperature-humidity structure of the lower atmosphere has been made at the Richard Aßmann Observatory Lindenberg (52.22°N, 14.12°E) of the German Weather Service since November 1998 by means of the 12 channel Radiometrics profiler TP/WVP 3000 (SOLHEIM et al., 1998; WARE et al., 2003). This more than 11 years long series is probably the longest series of this kind worldwide demonstrating convincingly the capability and feasibility of ground-based microwave profiling.

*Corresponding author: Dietrich Spänkuch, Schmerberger Weg 72, 14548 Schwielowsee / OT Caputh, Germany, e-mail: dietrichspaenkuch@web.de

0941-2948/2011/0222 $ 5.85
DOI 10.1127/0941-2948/2011/0222

In this paper we describe the passage of two dewpoint drops as particular mesoscale features similar to a dryline traced by MWRP in April 2007 at Lindenberg that has not been reported so far in Central Europe. Additional local information is used for the analysis from the 1290 MHz boundary layer radar wind profiler, the Ka-band cloud radar and surface instrumentation at the site. Maps of absolute humidity at the surface and of integrated water vapour (IWV) from the German GPS network show the development and dimension of this phenomenon in space and time.

2 Data sets

2.1 Microwave profiler

The MWRP measures atmospheric brightness temperatures at five frequencies from 22 to 30 GHz for water vapour profiling, and at seven channels from 51 to 59 GHz for temperature profiling, respectively. The data are provided with a temporal resolution of about one minute and are capable to resolve mesoscale features remaining often undetected by radiosondes. Profiles of temperature, water vapour density and liquid water are retrieved operationally using a neural network (NN) and an observation-based regression method (REGobs) including additionally zenith infrared and surface temperature, humidity and pressure sensors. The NN is trained on the basis of radiative transfer calculations using historical radiosonde soundings, and REGobs applies simultaneous observations (brightness temperature) of the MWRP and radiosondes from the past to calculate a regression operator. Neural networks are non-linear methods which provide profiles with a slightly higher vertical resolution. The REGobs operator is not affected by errors in the absorption model or instrumental bias, systematic deviations are considerably reduced. In spring the characteristic rms error of differences between MWRP retrievals and radiosondes is less than 1 K for temperature up to 1 km height and about 1.5 K between 1 and 3 km height. For vapour density the error increases up to $1\,g\,m^{-3}$ at 1 km and declines upward due to the lower amount of water vapour at these levels (GÜLDNER and LEPS, 2005). Nevertheless, ground-based microwave profiling enables monitoring of boundary layer processes during nearly all weather conditions in unattended mode. For this study the operationally archived 10-minutes mean values of NN retrievals were used. There was no reason to use REGobs retrievals.

2.2 Boundary Layer Radar Wind Profiler

Measurements of the mean horizontal wind were performed with a 1.29 GHz pulsed Doppler beam swinging Radar Wind Profiler (ENGELBART et al., 1996). The system was operated in a single resolution wind mode, using a 5-beam configuration (four tilted beams: North, South, West, East with 75° elevation and one vertical beam) with a pulse width of 700 ns (corresponding to a radial resolution of 100 m). The received signal was slightly oversampled in range with a 500 ns gate spacing (corresponding to a vertical range of 71.4 m). The transmitted pulse propagates along the different antenna directions which are sequentially switched one after the other. A small fraction of the transmitted energy is scattered back to the antenna. The two main echoing mechanisms for L-band Radar Wind Profilers are scattering at inhomogeneities of the refractive index (Bragg scattering) or at precipitation particles (Rayleigh scattering). After signal amplification, demodulation and A/D conversion, the Doppler spectrum of the receiving signal time series is estimated using standard Fast Fourier techniques, followed by the computation of the first three moments of the maximum energy peak: signal intensity (0. moment), radial velocity (1. moment) and spectral width (2. moment). A consensus avaraging of the radial wind estimates over 30 minutes discriminates atmospheric signals from noise peak estimates, and the resulting mean radial velocities are finally combined to obtain the three-dimensional wind vector. As usual, this assumes horizontal homogeneity of the wind field in the area spanned by the oblique beams over the averaging time period.

2.3 Cloud Radar

The Ka-band cloud radar MIRA 36 is a pulsed Doppler radar operating at a frequency of 35.5 GHz to measure vertical profiles of reflectivity, Doppler velocity as well as spectral width of meteorological targets in a height range between 150 m and 15 km (GÖRSDORF and HANDWERKER, 2006). The cloud radar transmits pulses of a length of 200 ns (corresponding to 30 m vertical resolution), and receives the signals backscattered by meteorological targets, like cloud droplets, drizzle doplets and ice crystals, but also by other particles, like insects. The signal processing contains a Fast Fourier transformation with 256 FFT points, and an averaging of 200 spectra (corresponding to an averaging time of 10 s). Normally the measuring quantities are used to determine cloud characteristics, like cloud base and cloud top as well as droplet distribution or liquid water content. In our case we use the cloud radar to determine the vertical velocity in the boundary layer although no clouds exist. In this case insects serve as targets assuming that they move passively with the wind. However, the assumption of passively moving insects in the wind field is not quite correct. Using this noncorrect assumption causes some bias in vertical velocity on the order of -0.2 to $-0.5\,m\,s^{-1}$ for updrafts, that is, a reduced updraft, and much smaller amounts for downdrafts as shown by several studies using different microwave frequencies, namely 915 MHz windprofiler data (ANGEVINE, 1997), 1238 MHz windprofiler and C-band Doppler radar radar measurements (LOTHON et al.,

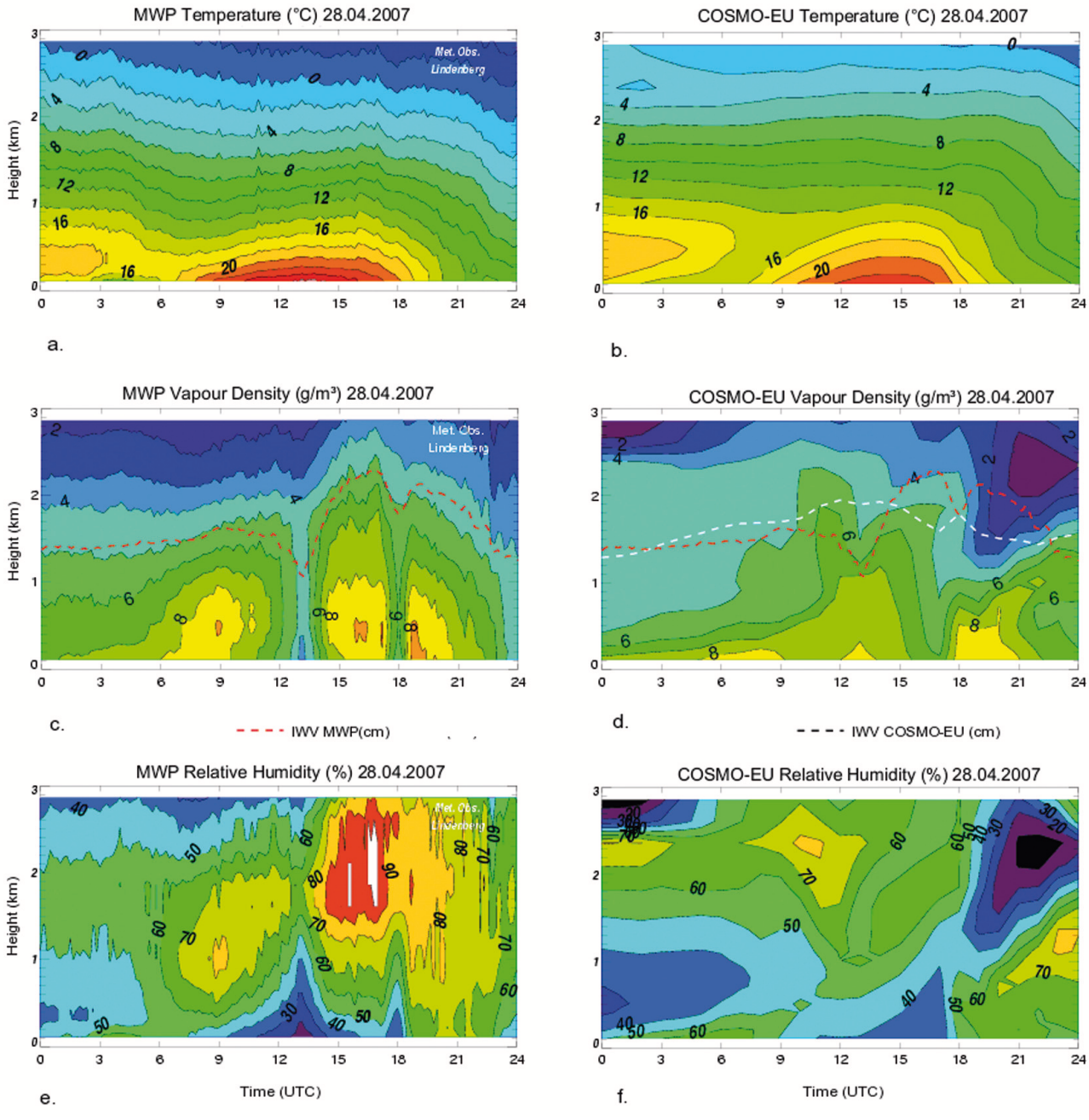

Figure 1: The daily course of temperature (top panel), vapour density (central panel), and relative humidity (lower panel) at Lindenberg on April 28, 2007 from MWP measurements (left panels) and corresponding to the NWP model COSMO-EU (right panels). The MWRP-derived IWV in cm is given as dashed red line in the central panels. The modeled IWV is given as white dashed line in the right central panel. Isolines are given in steps of 2 K for temperature, 1 g m^{-3} for vapour density and 10 % for relative humidity, respectively.

2009) and 95 GHz Doppler radar studies (GEERTS and MIAO, 2005). This bias is not relevant for our study, however. Due to the small measuring volume (0.5° antenna beam width corresponding to about 10 m horizontal range at 1 km) and the high velocity resolution (0.08 m s^{-1}) the radar is able to measure the small scale structure of the vertical velocity field.

2.4 GPS derived integrated water vapour

The GPS microwave signals are modified on their path through Earth's atmosphere leading to an additional signal path delay as compared with vacuum propagation. Special GPS processing techniques were developed to separate the path delays due to the neutral atmosphere and especially due to the water vapour and to estimate the integrated water vapour (IWV) above each individual GPS station (BEVIS et al., 1992). Since the begin-

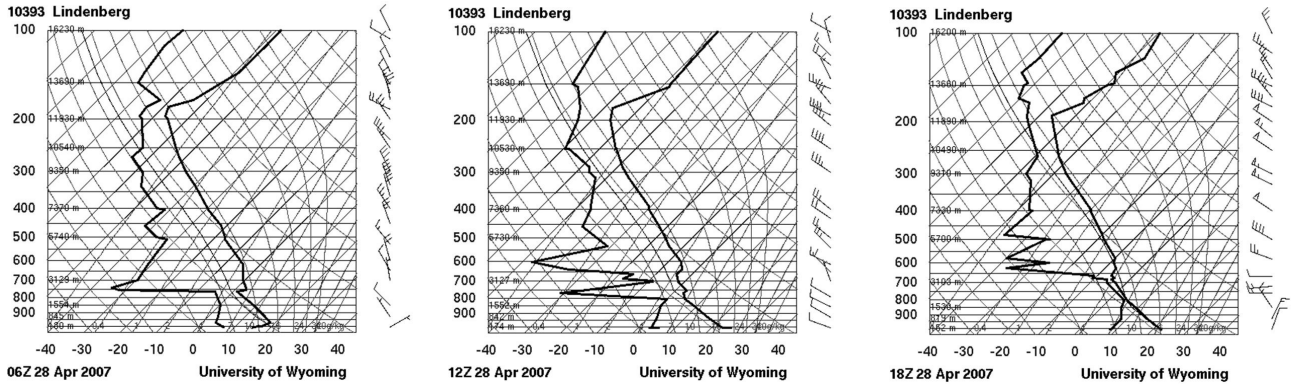

Figure 2: Skew T-log p plots at Lindenberg 0600(left), 1200(centre), and 1800(right). Note the very shallow near-surface superadiabatic layer of 20 m depth in the 1200 ascent. Reproduced by kind permission of the University of Wyoming, Department of Atmospheric Science.

Table 1: Hourly weather observations at Lindenberg on April 28, 2007 (extract)

Time (UTC)	T (°C)	RH (%)	Pressure (hPa)	Cloud observation octa, type, height(m)
10	23.9	39	1020.9	2, Ci fib, 9000
11	25.1	34	1020.4	<1, Cu tra, 1000
				<1, Ci fib, 9000
12	26.2	27	1019.7	1, Cu hum tra, 1500
13	26.6	20	1019.2	
14	26.4	23	1018.6	1, Cu med tra, 1200
				3, Ci-Cs fib, 6000
15	25.6	34	1018.0	3, Cu con med tra, 9000
				2, Ci fib, 8000
16	25.0	39	1017.7	2, Ci fib, 9000
17	23.0	44	1017.7	5, Cu con med tra, 2000
				2, Ac str tr, 3600
18	20.8	35	1018.0	3, Cu con med tra, 2000
				1, Ac tr, 3000
				2, Ci fib, 8000
19	18.3	62	1019.0	1, Cu con med, 2000
				2, Ac str tr, 3150
				2, Ci fib, 8000

ning of the last decade GPS-based IWV observations from large nationwide networks have been available on an operational basis (WARE et al., 2000). The German Research Center for Geosciences (GFZ) processes the data of about 350 German GPS stations operationally in near real-time and provides IWV observations with a temporal resolution of 15 minutes (DICK et al., 2001). IWV maps obtained from dense networks of GPS receivers give a detailed view on the spatiotemporal variation of water vapour.

Several validation studies comparing IWV obtained by GPS, by microwave radiometer, and by radiosonde showed mean differences of approximately 1 to 1.5 mm (GÜLDNER, 2001; GENDT et al., 2004; MARTIN et al., 2005). However, when comparing GPS-IWV with radiometer observations it should be kept in mind that several GPS observations along different satellite receiver axes are combined to estimate the IWV. The GPS-IWV is therefore an average over a radius of about 15 km around each GPS station and a period of 15 minutes. Spatial IWV variations of 10 % were found on this space scale at midlatitudes by KNEIFEL et al. (2009). The temporal variations might therefore be somewhat smoothed and delayed as compared with more pointlike observations provided by water vapour radiometers.

3 MWRP records and supporting observations at the site

On 28 April 2007 a dryline-like feature was observed by the MWRP as shown in the left panels of Fig. 1 presenting the course of temperature (top), vapour density (centre), and relative humidity (bottom) on that day. The right panels give the corresponding model outputs of the numerical weather prediction model COSMO-EU of the German Weather Service (STEPPELER et al., 2003). There are two sharp drops of vapour density without corresponding temperature drops as it is observed at drylines or dewpoint fronts, well known features in particular in the Southern Great Plains of the United States where moist and hot air from the Gulf of Mexico meets dry and hot air coming down from the Rocky Mountains. Drylines were also observed in northern India as a spatial stationar feature during the entire monsoon season (WESTON, 1972; CHIAO and BARROS, 2007) and in the northern part of the Australian continent as a regular nocturnal feature through the spring and summer (ARNUP and REEDER, 2007). Drylines are meso-gamma scale features in width (2-20 km) with a length of 500 to 1000 km (ZIEGLER et al., 1997). They are known as favoured zones of severe weather (RHEA, 1966; ZIEGLER and RASMUSSEN, 1998). The occurence of two humidity drops suggests even the passage of a double dryline (HANE et al., 1993; CRAWFORD and BLUESTEIN, 1997; DEMOZ et al., 2006).

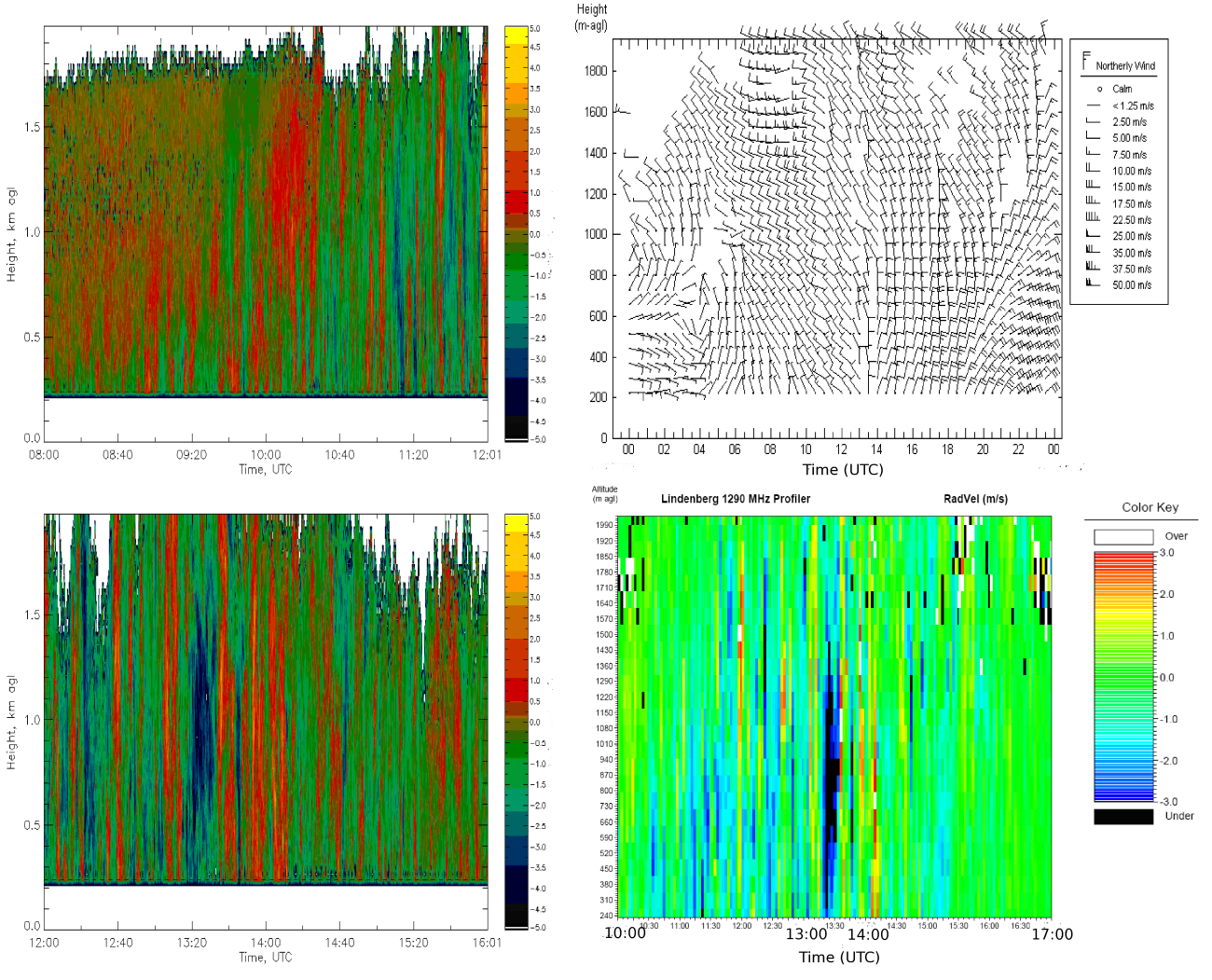

Figure 3: Vertical wind from the Ka-band cloud radar (left panel) from 0800 to 1200 UTC (top) and from 1200 to 1600 UTC (bottom) and horizontal (right upper panel) and vertical wind (right lower panel) from 1000 to 1700 UTC from the Boundary Layer Wind Profiler. 30 min averages.

The first humidity drop starts at about 1000 UTC (thereafter all times UTC) at the surface and is distinctly seen up to about 1 km. At about 1200 humidity decrease sets in too above that level drying the whole lower troposphere. The culmination of this drying event takes place between 1300 and 1400. The relative humidity drops to 17 % at the surface between 1303 and 1307 and is only slightly above 70 % between 1.5 and 2 km height. Significant humidity increase begins at all levels shortly before 1400 with 3 g m^{-3} within 1 hour in the lowest 800 m accompanied by cloud formation. A few single fair weather cumulus clouds were observed just before 1100 at 1000 to 1500 m height which were not caught by the MWRP and the ceilometer and disappeared after 1200 (see Table 1 for details of the weather observations). The hourly visual cloud observations are in our case more informative than the ceilometer measurements due to the small amount of cloudiness at that day as the weather observers see the whole sky and not only the zenith. Cumulus clouds are formed again at about 1500 at 2000 m with its largest amount of 5 octas two hours later indicating the passage of a frontal line at that time.

The second humidity drop of less intensity than the first one starts shortly after 1700 quasisimultaneously up to 2 km or even more and lasts for close upon one hour. There is a quasicontinuous moisture decline at greater heights till about 2230 when a further sharper humidity decrease is observed in the whole boundary layer. Both humidity drops were not caught by the radiosonde ascents made at this site every 6 hours as shown in Fig. 2. No pecularities are found in the temperature course (Fig. 1, top left). Only a marginal temperature increase of about 0.5 K above 2 km was retrieved dur-

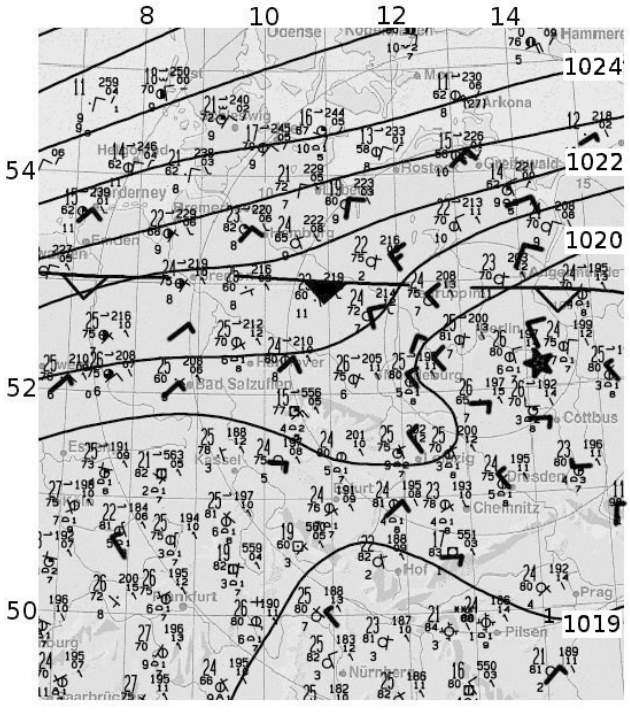

Figure 4: Surface weather chart on April 28, 2007 at 1200 UTC (Berliner Wetterkarte). Isobars are drawn in steps of 1hPa. Wind vectors follow the convention with full barb less than or equal $5\,\mathrm{m\,s^{-1}}$ and half barb equal or less than $2.5\,\mathrm{m\,s^{-1}}$, respectively. Notations on the left are northern latitude, on the top are eastern longitude, respectively. The Lindenberg site is indicated by a star.

ing the first humidity drop. A small temperature decrease is observed simultaneously with the second drop above about 300 m which strengthens with increasing height, but there is no discernible deviation in the decreasing temperature course at the surface during this event. Both humidity drops are reflected by the nonhydrostatic NWP model COSMO-EU to some extent but less pronounced than observed and shifted in time, however (Fig. 1, right central panel). The first drop occurs at the surface much stronger and about 2 hrs later than predicted. The model gives indeed humidity decrease at 1200 above 1 km but further increase below that altitude. The resulting modelled IWV, drawn as white dashed line in the central right panel of Fig. 1, shows thus only a marginal dip at that time in contrast to the observation. Another and probably more plausible interpretation of the model output is the following: The drying event aloft is exactly predicted in time but too weak to penetrate into the boundary layer up to the ground. The drying in the lowest hundred meters between 0900 and 1200 is due to evapotranspiration with moisture transport to higher levels explaining the steady modeled moisture increase at e.g. 500 m until about 1300. The temperature course is also by and large correctly given by the model but with a reduced daily amplitude, however. The real surface temperature is more than 2 K lower during early morning between 0300 and 0500 and higher by more than 2 K in maximum from 1000 and 1600. The model underestimates the temperature lapse rate distinctly except for the first four to five hours of the day. The deviations of temperature and vapour density between measurement and model output are enlarged in the field of relative humidity with too low values particularly after the passage of the first dew point drop (Fig. 1 bottom).

The development of the ABL during the day as shown in Figs.1 and 2 is typical for sunny summer days with a stable boundary layer (SBL) in the morning, caused by radiative cooling near the ground at night and subsequent transition to a convective boundary layer (CBL) driven by surface heating during daytime. The SBL had a depth of about 300 m at 0600 with a weak stable low tropospheric layer overhead. The 0600 ascent (Fig. 2, left panel) shows a remarkable sharp moisture drop within 250 to 300 m from $3.5\,\mathrm{g\,kg^{-1}}$ at 765 hPa to $0.28\,\mathrm{g\,kg^{-1}}$ at 740 hPa. The transition from SBL to CBL took place within about one hour between 0700 and 0800 according to the course of potential temperature θ (not given). Fig. 3, left panels, showing the registrations of the 10s vertical velocity from the Ka-band cloud radar is a good demonstration of the mixing process within the CBL. The rising thermals only marginally tilted if at all have in general a diameter of the order of 100 m and a depth of about 500 to 800 m with the exception of the thermal plume between 1000 and 1025 that had a diameter of about 4 km between about 1 and 1.5 km altitude. The CBL reached its final depth of about 1900 m at 1100. The 1200 ascent (Fig. 2 centre) shows a CBL of roughly constant θ of 296 K bounded by an extremely shallow superadiabatic layer of only about 20 m at the bottom where θ dropped by more than 2 K. This shallow superadiabatic layer is a challenge to every numerical model. The CBL was capped by a slight inversion of 2 K in θ. Moist air was advected above the CBL between 790 and 750 hPa in an about 400 m thick layer. Moistening of the CBL by $2\,\mathrm{g\,kg^{-1}}$ and more was observed till 1800.

The onset of humidity decrease at about 1000 is caused by downdraft of very dry air of about 5 % above 2 km corresponding to the radiosonde ascents of 0600 and 1200 at the site (Fig. 2), that is at that time when the boundary layer growth is rapid. MAHRT (1976) stated rapid boundary layer growth and rapid downward entrainment of dry air in case of weak stratification of the overlying free flow. The cloud radar data (Fig. 3, upper left panel) show that downdraft intervals with velocities around -1 $\mathrm{m\,s^{-1}}$ become superior to updraft intervals after about 1025. Strong downdraft with to about -5 $\mathrm{m\,s^{-1}}$ is observed after 1320 for about 15 min adequate to about 2.5 km horizontal extent (Fig. 3, lower panels) when the MWRP indicated the first significant humidity drop. The strongest downdraft is found between about 500 and 1500 m. This downdraft maximum is simultaneously connected with abating horizon-

tal winds of about 2.5 m s^{-1} in this height region and a wind shift from NW to N as shown by the 1290 MHz radar windprofiler data (Fig. 3, upper right panel). Combining both information from the cloud radar and the radar wind profiler the real wind blowed down a gentle SE slope of about 10° to the horizontal with a speed of about 6 m s^{-1} before the onset of the strong downdraft. With the onset of the strong downdraft the wind speed did not change very much but blowed down a steep southward looking slope of 65° to the horizontal between 500 and 1300 m and of 45° below that altitude. Updraft plumes suggesting gravity waves by their regular time spacing set in at about 1330 producing the clouds observed around 1400 as mentioned already. One possible explanation of increasing downdraft with simultaneous abating horizontal winds in flat terrain is the existence of a mesoscale low that sucks the surrounding air. The surface weather map (Fig. 4) does not show such a low, but indicates a slight convergence region near the site probably as a result of the downdraft. accompanied by some lowtropospheric wind shear. General pressure decline starts slowly at the site after 0600 with 0.1 to 0.2 hPa per hour when 1021.8 hPa were observed. Although the inter-hourly pressure fall intensified to 0.5 - 0.7 hPa between 1100 and 1600 resulting in 1017.7 hPa as minimum, no distinct dip is found in the general decline, however (see Table1). Pressure rise sets in at 1650 quasisimultaneously with the second humidity drop indicating the passage of a frontal system.

No remarkable pecularities in wind shift are observed during the onset of the first humidity drop at about 1000 but there is a slight and steady increase of 1 m s^{-1} per hour in wind speed at the surface from 1 m s^{-1} at 0900 to 4 m s^{-1} at 1200 followed by similar decrease till 1600. The wind direction went back by 50° from 350° to 300° between 1200 and 1300 indicating cold advection ahead of the front. There are also no noteworthy pecularities during the second humidity drop except the freshening of the wind in the lowest 2 km and the reversal of the pressure tendency as already mentioned.

4 Weather situation

A ridge of high pressure extending from the Azores to the Ukraine dominates the weather in Germany on April 28, 2007 with temperatures much above the climatological norm (24°C around noon except in mountain regions), large scale downdraft and mostly cloudless sky. The surface analysis at 1200 of the Berliner Wetterkarte (Fig. 4) shows a cold front over Northern Germany roughly at 53°N about 100 km north of the site as part of a strong low pressure system at the Pechora mouth in the northeastern corner of Europe. The cold front replaces continental tropical air by maritime polar air where isolated weak showers with marginal measurable precipitation were observed over southern Brandenburg and Saxonia in the evening and some more

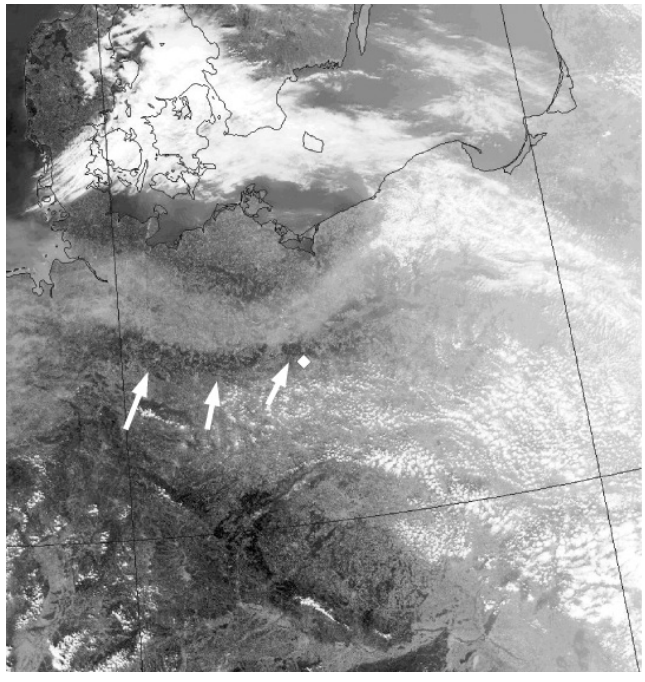

Figure 5: Channel 3 (459 to 479 nm) MODIS image of the AQUA satellite of April 28, 2007 at 1208 UTC. The Lindenberg site is indicated by a rhomb. The white arrows point to the swath of clear skies in front of the cold front seen as the grey band to the north. Drawn in are the 50°N latitude circle and the 10°E and 20°E longitude circles. This high resolution image was gratefully prepared by NEODAAS/University of Dundee.

rain in southern Poland. The front line is well seen in the channel 3 (459 to 479 nm) image of the Moderate Resolution Image Spectrometer (MODIS) of the AQUA satellite at 1208 as a diffuse somewhat structured band of moderate reflectivity of about 65 to 100 km width stretching from Pomerania across the North German Lowland until the German Bay (Fig. 5). The band located north of the site indicates enhanced aerosol optical depth and/or the existence of marginal partial cloudiness of subpixel size less than 250 m. South to the frontline there is east of about 9°E longitude a roughly 40 km times 300 km wide dark swath of cloudfree and aerosol poor atmosphere, indicated in Fig. 5 by white arrows, with many peninsulas of moderate reflectivity within. This dark swath is the region of enhanced downdraft in front of the cold front. The pattern described is not seen in the AVHRR images at 1033 and only sligthly detectable in the AVHRR channel 1 (580 to 680 nm) image at 1323 UTC and in the Meteosat IR channel at 1200 (Berliner Wetterkarte 56, April 2007). There is north to the diffuse band of moderate reflectivity another dark region indicating clear sky behind the front that extends beyond the coastline of the Baltic Sea. The development in the midtroposphere on April 28 is displayed in Fig. 6 taken from http://www.wetter3.de/Archiv where many other maps of several meteorological parameters at every six hours are compiled. Given are the 500 hPa geopotential height in black lines, the 500–1000 hPa thickness

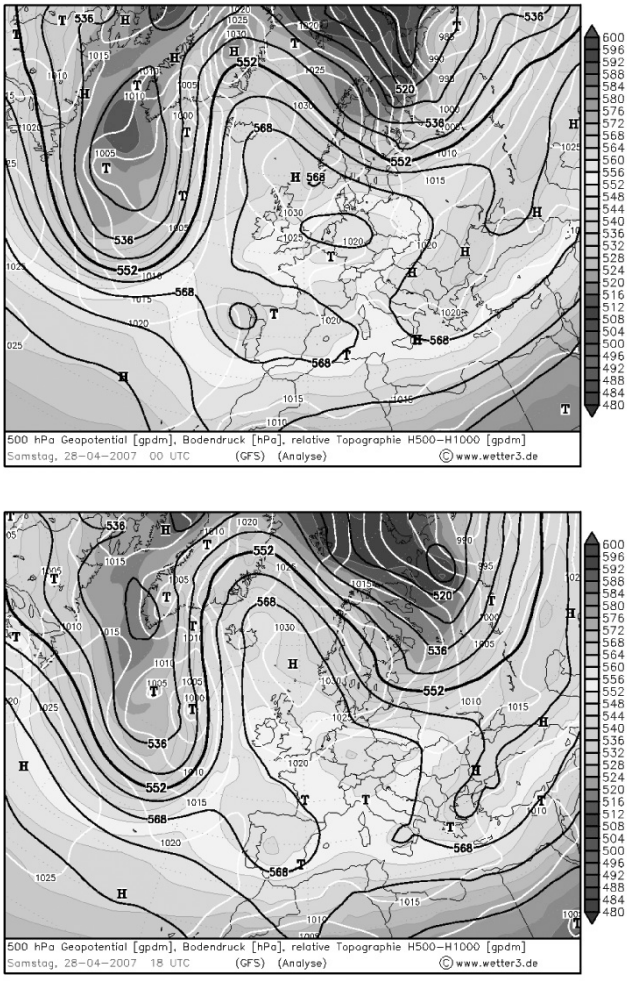

Figure 6: 500 hPa geopotential height (black lines), 500–1000 hPA thickness (grey shading), and surface pressure (white lines) on April 28, 2007 for 0000 UTC (top) and 1800 UTC (bottom). Kind permission of wetter3.de.

in grey shading, and the surface pressure field in white lines for 0000 (top) and 1800 (bottom). Central Europe had been dominated for several days by the midtropospheric high that laid at 0000 above Germany with more than 574 gpdm. Eighteen hours later, the high was dissolved, and a high pressure ridge where the midtropospheric high was imbedded in had extended to the north beyond Iceland. The degration of the midtropospheric high was due to outflow of dry air at its edges that caused the observed downdrafts at the site. This outflow was accompanied by some windshear as seen in Fig. 3. There was no significant thickness advection during that time.

5 Development of the features in space and time

There are a couple of questions that cannot be answered by local measurements like origin, development, migration and lifetime of the features described. It needs additional information of meteorological parameters in space and time to give adequate answers. Two different data sources are capable of useful information: meteorological parameters at the surface available every hour from the regular meteorological network and IWV maps derived from GPS data every 15 min. There were no further suitable information from satellite images that could be added to the MODIS image (Fig. 5). Surface weather is per se more influenced by the underlying boundary in particular in mountain regions than integral atmospheric parameters like IWV. Nevertheless, the downdraft events detected by screening of the routinely made MWRP records should clearly be seen in the surface maps too. The field of absolute humidity at the surface proved to be the most informative data source. Fig. 7 gives a set of maps of this parameter beginning with the field at 1000 (Fig. 7a) when the drying at the site, indicated by a cross in the Figure, sets in. At this time, the site was located in a ridge of enhanced vapour density of slightly more than $8\,\mathrm{g\,m^{-3}}$. A streak of reduced water vapour with amounts less than $7\,\mathrm{g\,m^{-3}}$ is seen northwest of the site with two pronounced kernels of local vapour minima of less than $5\,\mathrm{g\,m^{-3}}$ in a distance of roughly 140 km from each other. This streak corresponds with the dark swath of the MODIS image (Fig. 5). It indicates the downdraft zone in front of the approaching cold front. The sequence of the maps of Fig. 7 shows that one of the kernels of this downdraft zone is equivalent to the first humidity drop. Both kernels united after 1100 (not shown) and formed a narrow stripe of about 70 km length in west-east direction about 70 km WNW of Lindenberg at 1200 (Fig. 7b). The stripe divided again after 1200 into two kernels, one of them at the site, the other more intense one about 140 km apart from and west of Lindenberg at 1300 (Fig. 7c). Both kernels approach each other by migration of the western one in southeast direction and of the eastern one at Lindenberg in southwest direction between 1300 and 1400, the time of the culmination of the first downdraft. They are at 1400 UTC located at 52.2°N about 70 km apart at 12.5°E and 13.5°E southwest of Lindenberg (Fig. 7d). Both kernels weakend during the next hour between 1400 and 1500 (Fig. 7e), the western kernel moved eastward to the position of the eastern kernel and the weaker one to the southeast, both with a speed of about 70 km per hour. Further weakening at least of the western kernel (the other kernel moved out of the map section) took place with reduced velocity of about 40 km per hour in direction southeast between 1500 and 1600 (not shown) followed by strengthening again with unchanged speed in the same direction during the following hour so that the downdraft cell was located about 60 km SSE from the site at 1700 (Fig. 7f). The kernel deceased between 1800 and 1900 slightly south of the 1700 position.

The origin of the downdraft cells could be fixed too. The western cell that developed to the stronger one during the day is seen in the 0900 map (not shown) as a region of slightly reduced water vapour as the

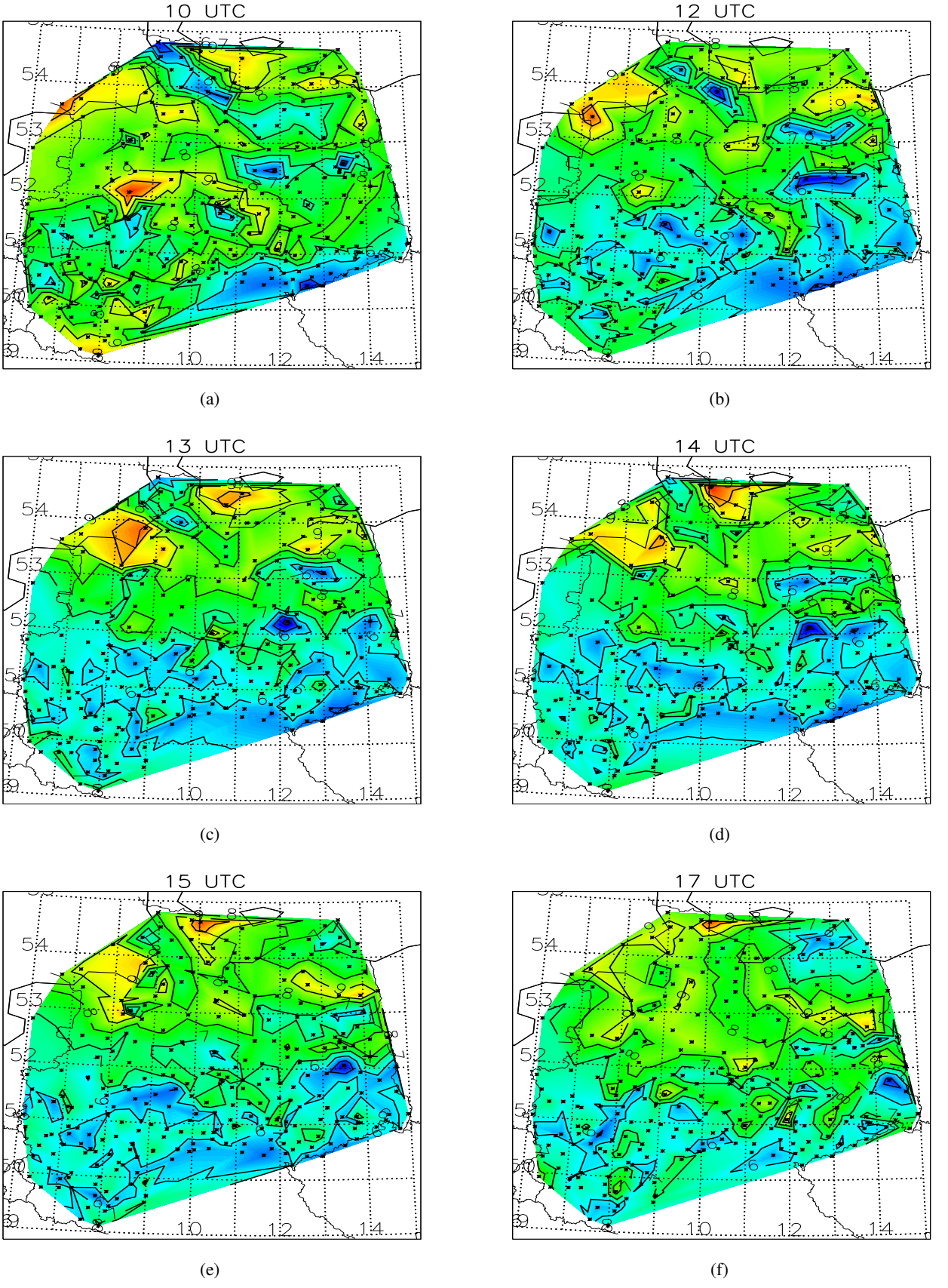

Figure 7: Maps of near-surface distributions of absolute humidity on 28 April 2007at different times. Upper row 1000 UTC (a), 1200 UTC (b), central row 1300 UTC (c), 1400 UTC (d) and lower row 1500 UTC (e) 1700 UTC (f). The site is marked by a cross. Isolines are given in steps of 1 g m^{-3}

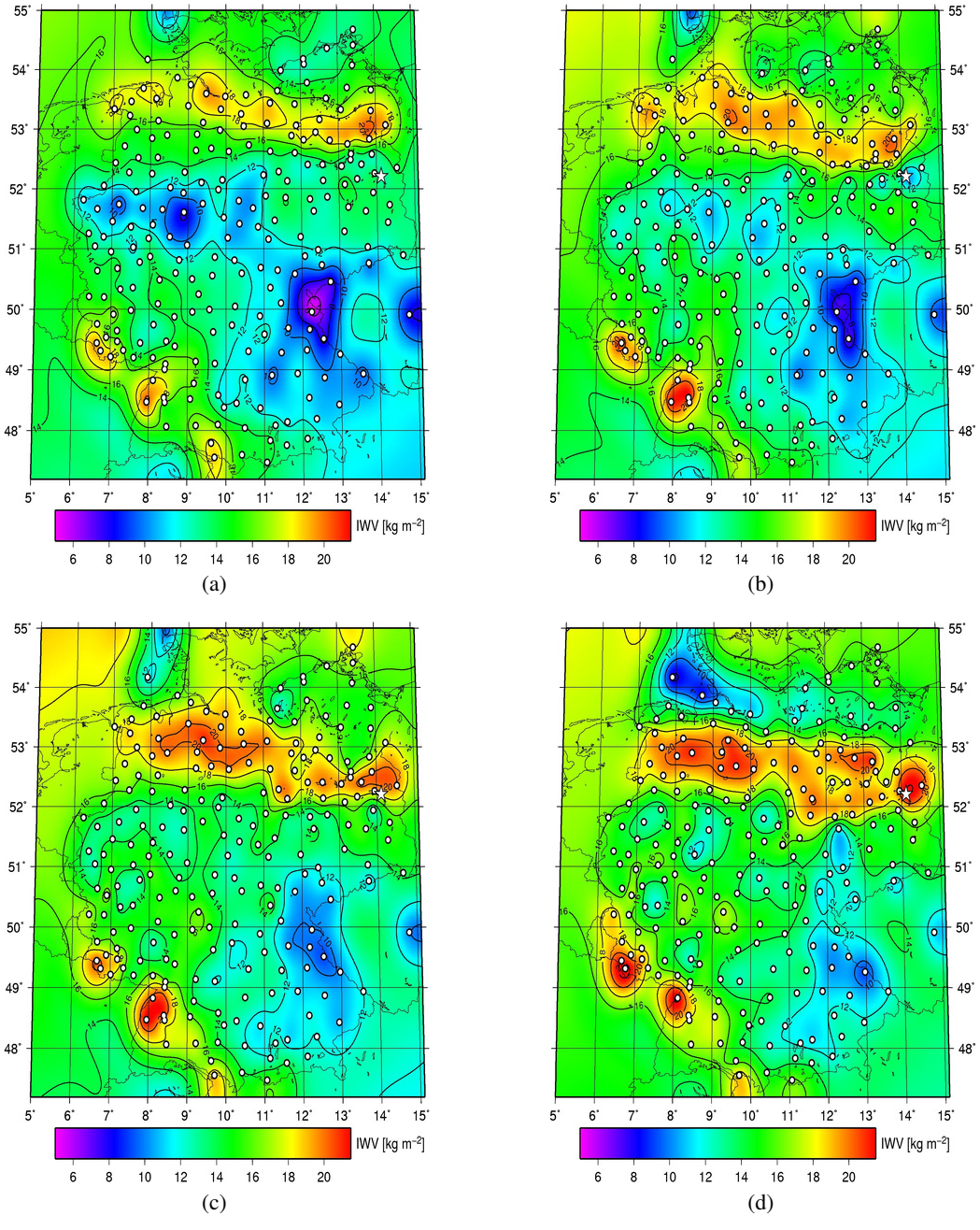

Figure 8: Maps of Integrated Water Vapour at 1007(a), 1307(b), 1507(c) and 1707(d) UTC. Indicated are the GPS stations. The Lindenberg site is marked by a star. Isolines ae given in IWV steps of 2 kg m^{-2} equivalent to 2 mm ppw.

same position as at 1000. The other cell, also at the same position as one hour later, was well developed already at that time with amounts less than 7 g m^{-3}. The lifetime of the downdraft cells was thus somewhat more than 9 hours. The place of death of the western cell is about 180 km southeast of its place of birth, the total covered distance is larger, however, due to its partly nonrectilinear movement. The cells were nearly fixed during the first and last hour of their life. The maximum velocity was about 70 km hr^{-1} during their climax.

Fig. 7 is also used to investigate the history of the second humidity drop. It approaches the site at 1700 as the remnant of the postfrontal dry zone that extended across northern Germany during the morning hours from Schleswig-Holstein to the Uckermark northeast of Berlin. This dry zone is located at the eastern side of the deceasing high at 500 hPa (Fig. 6) and is thus caused by the outflow of dry and cold air coming from this high. The sequence of the maps of Fig. 7 shows clearly the weakening of this zone and its disintegration into single cells during the day due to undermined outflow from the weakened high. There is only one cell left from this drying zone at 1700. This cell was nearly stationary for about three hours between 1200 and 1500

and moved afterwards southward with a speed of about 40 km per hour.

The migration of the patterns in the surface humidity field excludes local causes and suggests downdrafts like observed at Lindenberg as plausible cause. All humidity minima of the surface humidity field were without exception not accompanied by temperature changes. The decline in surface humidity at the site down to 17 % was also not the strongest one. The absolute minimum was observed with 14 % relative humidity 150 km to the west at 1300.

The downdraft cells are also detectable in the maps of IWV in particular at 1307 (Fig. 8b) where two seperate cells with minima less than 12 mm are seen at Lindenberg and somewhat west of the site. Both cells were also first seen like in the surface vapour density map at 0907 (not shown). The features in the IWV maps are generally less pronounced than in the surface humidity maps, however. On the other hand, the position of the front at the surface is more clearly definable in the IWV map than by the classical meteorological parameters as the IWV gradient is significantly stronger than the temperature gradient and the wind field too weak to determine a distinct wind shift. The marginal cloudiness in the region giving no information was mentioned already. As fronts are often not well-defined features (MASS, 1991; SANDERS and DOSWELL, 1995; SANDERS, 1999) the capability of IWV in improving frontal analysis is worthwhile for further studies.

The belt of enhanced IWV of more than 18 mm with three more or less pronounced maxima above 20 mm corresponds well with the diffuse band of enhanced optical depth of the MODIS image (Fig. 5). The maximum IWV gradient defines the position of the frontline. Less pronounced than in the MODIS image is the dark belt of low optical depth in front of the frontline, however. There is a general decrease of IWV from north to south from amounts of about 20 mm in maximum to partly less than 10 mm in central and southern Germany. The IWV maps show like the surface maps many mesoscale features. Their analysis and discussion is however beyond the scope of this paper and needs further research.

6 Discussion

The combined analysis of ground-based microwave, windprofiler and cloud radar measurements at the site and of data of the surface meteorological network and of the national GPS network show the different nature of two dryline-like humidity drops observed on the same day in April 2007 in Lindenberg. The first humidity drop is induced by strong downdraft and is the result of strong mixing of thermal plumes from below and dry air entrained from above. Slight convergence near the surface with lowtropospheric windshear advects cold dry air ahead of the front. The second humidity drop is caused by replacement of continental tropical air by maritime polar air of nearly the same temperature when it arrived at the site due to strong solar insolation during the day. The second event is thus not caused by subsidence, rather than by dry advection behind the front.

The downdraft that caused the first humidity drop had a slope of 45° to 65° to the horizontal at maximum at the site with a speed of $7\,\mathrm{m\,s^{-1}}$ and travelled by and large parallel to and about 40 km in front of the frontline with variable speed. It meets the criterion of a dryline with its gradient of specific humidity larger than $3\,\mathrm{g\,kg^{-1}}$ per 100 km (HOCH and MARKOWSKI, 2005) equivalent to about $3.5\,\mathrm{g\,m^{-3}}$ per 100 km of vapour density or larger than 7.5 mm per 100 km of IWV when the well-known relation IWV=2.16 ρ_s is applied with ρ_s the vapour density at the surface in $\mathrm{g\,m^{-3}}$ (e.g., MÖLLER and BULLRICH (1961)). It meets the condition of a line only partly, however. Although there seems to exist a line from time to time, e.g., at 1400 and 1500 (Fig. 7), the humidity-gradient-criterion is not fulfilled for a great part of this feature. The greatest length of the line meeting the criterion of the humidity gradient was estimated to be a bit more than 200 km compared to the 500 to 1000 km length of the drylines in the Great Plains. The smaller length of the line in northern Germany is not surprising, however, considering the differences in nature and scale of the two landscapes. Most of the time the humidity-gradient-criterion was met only by the two prefrontal kernels within the zone of reduced moisture and not by the whole zone. The maximum size of one cell was found to about 70 km x 38 km at 1400. The horizontal dimension of the downdraft plume in Lindenberg is estimated to 18 to 32 km in north-south direction using the measured wind velocity of $5\,\mathrm{m\,sec^{-1}}$ at the site. Prefrontal features associated with cold fronts are not uncommon. An excellent overview of such features and their responsible mechanisms is given in the review paper of SCHULTZ (2005). The size of the second humidity drop at 1700, that also meet the humidity-gradient-criterion was about 40 km in meridional direction in agreement with the estimate made by the local wind measurements and about 230 km in west-east direction according to Fig. 7.

Drylines are regular seasonal features in low latitude regions of the world above sloped terrain like in the Great Plains of the United States and in India, or above flat terrain like in northern Australia where they develop at the boundary between tropical maritime and continental air masses over the heated continent from a sea-breaze circulation. Both preconditions – sloped terrain or sea-breaze circulation – are not given in our case. There is weak cyclonal circulation near the surface around the site with weak winds ahead the front (Fig. 4). The wind profiler data (Fig. 3, upper right panel) show that the wind did not change with height very much, except at around 1300, but the wind direction tended to back with height, suggestive of cold advection both ahead and behind the front due to low-level wind shear.

SUN and WU (1992) investigating dryline formation during fair weather found dryline strength most sensitive to low-level wind shear, large-scale terrain slope, and volumetric soil moisture gradients, in that order. There are many lakes and forests around the site. Significant moisture gradients at the surface are thus per se given. The occurrence of kernels are thus plausible as well as their partly irregular migration.

The predominance of local kernels or cells within the prefrontal drying zone suggests the term dry cell or dry kernel. It is justified from our point of view to consider the two dry cells found in the surface humidity field as well as in the IWV field as individuals because they move partly independent from each other. They approach each other, unify for a certain time and separate in their lifetime of a bit more than 9 hours. Detailed structures in the horizontal along-line direction of drylines, in the mesoscale in particular horizontal convective rolls in more or less regular spacing (BLUESTEIN et al., 1988) are common and have been extensively investigated by sophisticated field experiments in the Great Plains (HANE et al., 1993; ATKINS et al., 1998; DEMOZ et al., 2006).

It is worthwhile mentioning that the drying event was predicted to some extent by the numerical weather prediction model (Fig. 1). All in all, the term dryline-like is from our point of view the adequate description of the phenomenon discussed rather than the term dryline as the first dry zone consisted in particular in the two downdraft kernels or cells that caused the dew-point drops. These cells were more or less independent individuals.

7 Conclusions

The detailed analysis of two humidity drop events without corresponding temperature changes detected by the ground-based microwave radiometer profiler at Lindenberg in the Northern German Lowlands showed that the first and more intense drop was caused by severe downdraft in front of a cold front. Measurements of the synoptic surface network and GPS derived IWV data were indispensable analysis tools to show the prefrontal downdraft region as consisting in particular of two pronounced mesoscale downdraft kernels of variable size and shape with a lifetime of a bit more than 9 hours. The second humidity drop in the afternoon was caused by advection of dry air behind the front with nearly the same temperature as the previous air. The phenomenon described has many features of a dryline and is, so far as we know, the first one observed in Central Europe. This study shows convincingly the role ground-based passive microwave profiling can play in concert with other sophisticated remote sensing systems in operational monitoring of mesoscale ABL processes. Its all weather feasibility is particular attractive for such studies.

Acknowledgments

We would like to thank Ulrich Görsdorf, Volker Lehmann (both at the Richard-Aßmann-Observatory Lindenberg), and Werner Wehry (Free University Berlin) for their input and discussions as well as Jörg Liebing (Regionale Messnetzgruppe Potsdam des DWD) for providing the data of the surface network. The authors acknowledge the constructive comments of two anonymous referees. We appreciate the support of NEODAAS/University of Dundee for providing the MODIS image (Fig. 5). The first author is indebted to the German Weather Service for support.

References

ANGEVINE, W.M., 1997: Errors in mean vertical velocities measured by boundary layer wind profilers. – J. Atmos. Oceanic Technol. **14**, 265–269.

ARNUP, S.H., M.J. REEDER, 2007: The diurnal and seasonal variation of the northern Australian dryline. – Mon. Wea. Rev. **135**, 2995–3008.

ATKINS, N.T., R.M. WAKIMOTO, C. L. ZIEGLER, 1998: Observations of the finescale structure of a dryline during VORTEX 95. – Mon. Wea. Rev. **126**, 525–550.

BEVIS, M. S., BUSINGER, T. A. HERRING, C. ROCKEN, R.A. ANTHES, R.H. WARE, 1992: GPS meteorology: Remote sensing of atmospheric water vapor using the global positioning system. – J. Geophys. Res. **97**, 15787–15801.

BLUESTEIN, H.B., E.W. MCCAUL JR., G. P. BYRD, G.R. WOODALL, 1988: Mobile sounding observations of a tornadic storm near the dryline: The Canadian, Texas storm of 7 May 1986. – Mon. Wea. Rev. **116**, 1790–1804.

CHIAO, S., A.P. BARROS, 2007: A numerical study of the hydrometeorological dryline in northwest India during the monsoon. – J. Met. Soc. Japan **85A**, 337–361.

CRAWFORD, T.M., H.B. BLUESTEIN, 1997: Characteristics of dryline passage. – Mon. Wea. Rev. **125**, 463–477.

DEMOZ, B., and Co-authors, 2006: The dryline on 22 may 2002 during IHOP_2002: Convective scale measurements at the profiling site. – Mon. Wea. Rev. **134**, 294–310.

DICK, G., G. GENDT, C. REIGBER, 2001: First experience with near real-time water vapor estimation in a German Gps network. – J. Atmos. Solar-Terrest. Phys. **63**, 1295–1304.

ENGELBART, D., H. STEINHAGEN, U. GÖRSDORF, J. LIPPMANN, J. NEISSER, 1996: A 1290 MHz profiler with RASS for monitoring wind and temperature in the boundary layer. – Beitr. Phys. Atmos. **69**, 63–80.

GEERTS, B., Q. MIAO, 2005: The use of millimeter Doppler Radar echoes to estimate vertical air velocities in the fair-weather convective boundary layer. – J. Atmos. Oceanic Technol. **22**, 225–246.

GENDT, G., G. DICK, C. REIGBER, M. TOMASSINI, Y. LIU, M. RAMATSCHI, 2004: Near real time GPS water vapor monitoring for numerical weather prediction in Germany. – J. Meteor. Soc. Japan **82**, 361–370.

GÖRSDORF, U., J. HANDWERKER, 2006: A 36 GHz high sensitivity cloud radar for continuous measurements of cloud parameters – experiences of 2-years operation and system intercomparison. – In: Proceedings of the 7th International Symposium on Tropospheric Profiling; Needs and Technologies, Boulder, 12.–16.06.2006.

GÜLDNER, J., 2001: Validation of integrated water vapor using independent measurement techniques. – Phys. Chem. Earth **26**, 427–431.

GÜLDNER, J., J.-P. LEPS, 2005: Analysis of CLIWA-NET intensive operation period data as part of the monitoring activities at the German Meteorological Service site Lindenberg. – Atmos. Res. **75**, 151–166.

GÜLDNER, J., D. SPÄNKUCH, 2001: Remote sensing of the thermodynamic state of the atmospheric boundary layer by ground-based microwave radiometry. – J. Atmos. Oceanic Technol. **16**, 925–933.

GÜLDNER, J., A. CHRISTOPH, D. ENGELBART, M. E. FERRARIO, C. HERET, U. LÖHNERT, F. MADONNA, D. RUFFIEUX, C. WRENCH, Y. ZOLL, 2009: Towards the comparability of microwave observations: Results from a temporary profiler network during the WMO campaign LUAMI in November 2008. – In: APITULEY, A., H.W.J. RUSSCHENBERG (Eds.), Proceedings of the 8th International Symposium on Tropospheric Profiling, ISBN 978-90-6960-233-2 Delft, The Netherlands, October 2009.

HANE, C.E., C.L. ZIEGLER, H.B. BLUESTEIN, 1993: Investigation of the dryline and convective storms initiated along the dryline: Field experiments during COPS-91. – Bull. Amer. Meteor. Soc. **74**, 2133–2145.

HEWISON, T., 2007: 1D-VAR retrievals of temperature and humidity profilesfrom a ground-based microwave radiometer. – IEEE Trans. Geosci. Remote Sens. **45**, 2163–2168.

HOCH, J., P. MARKOWSKI, 2005: A climatology of springtime dryline position in the U.S. Great Plains region. – J. Climate **18**, 2132–2137.

ILLINGWORTH, A. J., AND, CO-AUTHORS, 2007: CLOUDNET: Continuous evaluation of cloud profiles in seven operational models using ground-based observations. – Bull. Amer. Meteor. Soc. **88**, 883–898.

KNEIFEL, S., S. CREWELL, U. LÖHNERT, J. SCHWEEN, 2009: Investigating water vapor variability by ground-based microwave radiometry: Evaluation using airborne observations. – IEEE Geosci. Rem. Sens. Letters **6**, 157–161, DOI:10.1109/LGRS.2008.2007659.

KNUPP, K., R. WARE, D. CIMINI, F. VANDENBERGHE, J. VIVEKANANDAN, E.R. WESTWATER, T.COLEMAN, 2009: Ground-based passive microwave profiling during dynamic weather conditions. – J. Atmos. Oceanic Technol. **26**, 1057–1073.

LÖHNERT, U., S. CREWELL, C. SIMMER, 2004: An integrated approach toward retrieving physically consistent profiles of temperature, humidity, and cloud liquid water. – J. Appl. Meteor. **43**, 1295–1307.

LOTHON, M., B. CAMPISTRON, S. JACOBI-KOALY, F. LOHOU, F. GIRARD-ARDHUIN, 2009: Comparison of radar reflectivity and vertical velocity observed with a scannable C-band radar and two UHF profilers in the lower troposphere. – J. Atmos. Oceanic Technol. **19**, 899–910.

MAHRT, L., 1976: Mixed layer moisture structure. – Mon. Wea. Rev. **104**, 1403–1407.

MARTIN, L., C. MÄTZLER, T.J. HEWISON, D. RUFFIEUX, 2005: Intercomparison of integrated water vapour measurements. – Meteorol. Z. **15**, 57–64.

MASS, C.F., 1991: Synoptic frontal analysis: Time for a reassessment? – Bull. Amer. Meteor. Soc. **72**, 348–363.

MÖLLER, F., K. BULLRICH, 1961: Thermodynamische Grundlagen und Arbeitsmethoden der Aerologie – In: HESSE, W.: Handbuch der Aerologie, Akademische Verlagsgesellschaft Geest & Portig, Leipzig,34.

RHEA, J.O., 1966: A study of thunderstorm formation along the dryline. – J. Appl. Meteor. **5**, 58–63.

SANDERS, F., 1999: A proposed method of surface map analysis. – Mon. Wea. Rev. **127**, 945–955.

SANDERS, F., A. C. DOSWELL, 1995: A case for detailed surface analysis. – Bull. Amer. Meteor. Soc. **76**, 505–521.

SCHULTZ, D.M., 2005: A review of cold fronts with prefrontal troughs and wind shifts. – Mon. Wea. Rev. **133**, 2449–2472.

SOLHEIM, F., J.R. GODWIN, E.R. WESTWATER, Y. HAN, S.J. KEIHM, K. MARSH, R. WARE, 1998: Radiometric profiling of temperature, water vapor and cloud liquid water using various inversion methods. – Radio Sci. **33**, 393–404.

STEPPELER, J., G. DOMS, U. SCHÄTTLER, H. BITZER, A. GASSMANN, U. DAMRATH, G. GREGORIC, 2003: Meso-gamma scale forecasts using the nonhydrostatic model LM. – Meteor. Atmos. Phys. **82**, 79–93.

SUN, W.Y., C.C. WU, 1992: Formation and diurnal variation of a dryline. – J. Atmos. Sci. **49**, 1606–1619.

TURNER, D. D., 2007: Improved ground-based liquid water path retrievals using a combined infrared and microwave approach. – J. Geophys. Res. **112**, D15204, doi:10.1029/2007JD008530.

WARE, R.H., D.W. FULKER, S.A. STEIN, D.N. ANDERSON, S. K. AVERY, R.D. CLARK, K.K. DROEGEMEIER, J. P. KUETTNER, J.B. MINSTER, S. SOROOSHIAN, 2000: SuomiNet: A real-time national GPS network for atmospheric research and education. – Bull. Amer. Meteor. Soc. **81**, 677–694.

WARE, R., R. CARPENTER, J. GÜLDNER, J. LILJEGREN, T. NEHRKORN, F. SOLHEIM, F. VANDENBERGHE, 2003: A multi-channel radiometric profiler of temperature, humidity, and cloud liquid. – Radio Sci. **38**, 8079, doi:10.1029/2002RS002856.

WESTON, K.J., 1972: The dry-line of northern India and its role in cumulonimbus convection. – Quart. J. Roy. Meteor. Soc. **98**, 519–531.

WESTWATER, E.R., S. CREWELL, C. MÄTZLER, 2005: Surface-based microwave and millimeter wave radiometric remote sensing of the troposphere: a tutorial. – IEEE Geosci. Remote Sens. Soc. Newslett. **134**, 16–33.

ZIEGLER, C.L., T.J. LEE, R.A. PIELKE SR, 1997: Convective initiation at the dryline: A modeling study. – Mon. Wea. Rev. **125**, 1001–1026.

ZIEGLER, C.L., E.N. RASMUSSEN, 1998: The initiation of moist convection at the dryline: Forecasting issues from a case study perspective. – Wea. Forecast. **13**, 1106–1131.